Nickel telluride as a bifunctional electrocatalyst for efficient water splitting in alkaline medium

Journal:	*Journal of Materials Chemistry A*
Manuscript ID	TA-ART-02-2018-001760.R1
Article Type:	Paper
Date Submitted by the Author:	17-Mar-2018

Complete List of Authors:	DeSilva, Umanga; Missouri University of Science & Technology, Chemistry Masud, Jahangir; Missouri University of Science and Technology, Chemistry Zhang, Ning; Missouri University of Science & Technology, Materials Science & Engineering Hong, Yu; Missouri University of Science and Technology, Materials Science & Engineering Liyanage, Wipula; Missouri University of Science and Technology, Chemistry Asle Zaeem, Mohsen; Missouri University of Science and Technology, Materials Science and Engineering Nath, Manashi; Missouri University of Science & Technology, Chemistry

Journal Name

ARTICLE

Received 00th January 20xx,

Accepted 00th January 20xx

DOI: 10.1039/x0xx00000x

www.rsc.org/

Nickel telluride as a bifunctional electrocatalyst for efficient water splitting in alkaline medium

Umanga De Silva,[a] Jahangir Masud,[a] Ning Zhang,[b] Yu Hong,[b] Wipula P. R. Liyanage,[a] Mohsen Asle Zaeem,[b] Manashi Nath[a]*

Designing efficient electrocatalysts has been one of the primary goals for water electrolysis, which is one of the most promising routes towards sustainable energy generation from renewable sources. In this article, we have tried to expand the family of transition metal chalcogenide based highly efficient OER electrocatalysts by investigating nickel telluride, Ni_3Te_2 as a catalyst for the first time. Interestingly Ni_3Te_2 electrodeposited on GC electrode showed very low onset potential and overpotential at 10 mA cm^{-2} (180 mV), which is the lowest in the series of chalcogenides with similar stoichiometry, Ni_3E_2 (E = S, Se, Te) as well as Ni-oxides. This observation falls in line with the hypothesis that increasing covalency around the transition metal center enhances catalytic activity. Such hypothesis has been previsouly validated in oxide-based electrocatalysts by creating anion vacancies. However, this is the first instance where this hypothesis has been convincingly validated in the chalcogenide series. The operational stability of the Ni_3Te_2 electrocatalyst surface during OER for extended period of time in alkaline medium was confirmed through surface-sensitive analytical techniques such as XPS, as well as electrochemical methods which showed that the telluride surface did not undergo any corrosion, degradation, or compositional change. More importantly we have compared the catalyst activation step ($Ni^{2+} \rightarrow Ni^{3+}$ oxidation) in the chalcogenide series, through electrochemical cyclic voltammetry studies, and have shown that catalyst activation occurs at lower applied potential as the electronegativity of the anion decreases. From DFT calculations we have also shown that the hydroxyl attachment energy is more favorable on the Ni_3Te_2 surface compared to the Ni-oxide, confirming the enhanced catalytic activity of the telluride. Ni_3Te_2 also exhibited efficient HER catalytic activity in alkaline medium making it a very effective bifunctional catalyst for full water splitting with a cell voltage of 1.66 V at 10 mA cm^{-2}. It should be noted here that this is the first report of OER and HER activity in the family of Ni-tellurides.

1. Introduction

The intensive search for sustainable alternative energy and clean fuel has intensified research activities in the energy sector.[1,2] Amongst the various technologies for alternative energy generation and storage, catalytic water splitting has been at the center of attention for decades.[3] Water electrolysis typically involves two half cell reactions, oxygen evolution reaction (OER) occurring at the anode and hydrogen evolution reaction (HER) occurring at the cathode.[4] Among these OER is a more challenging step involving an uphill complex proton-coupled electron transfer reaction (PCET) which leads to this step being kinetically sluggish and typically requires a high overpotential to get over the energy barrier.[5] Hence, anodic catalysts are typically used to reduce the overpotential for OER and increase the output current density. Traditionally precious metal oxides such as RuO_2 and IrO_2 exemplified the most active catalysts for OER in alkaline and acidic medium, respectively.[6,7] However, the scarcity and rising costs of the noble metals have led to the continuous quest for replacing these precious metals with earth abundant, non-precious metals without compromising catalytic efficiency. This quest has been rewarded over the last couple of years by the discovery of several transition metal based OER electrocatalysts, specifically those containing Ni, Co, and Fe.[4,8-24] Although, the transition metal based OER electrocatalysts has been over-represented with oxides[4,20,22,25], during the last couple of years sulfides[26-29] selenides[14,16,17,19,21,24,30-34] and pnictides[35-40] have shown unprecendented high catalytic activity, some of which even surpasses that of the corresponding oxides. In fact, the trend in catalytic activity between the oxides and the rest of the chalcogenide series (sulfides, selenides, and tellurides) can be best explained through the gradual change in their electronic band structure and alignment of the valence and conduction band edges with the water oxidation-reduction levels.[41,42] As the electronegativity of the chalcogen atom decreases down the series, degree of covalency in the metal-chalcogen bond increases. Based on previous research which has shown that OER catalytic efficiency is enhanced by higher degree of

---

[a] *Department of Chemistry, Missouri University of Science and Technology, Rolla, MO 65409.*

[b] *Department of Materials Science & Engineering, Missouri University of Science & Technology, Rolla, MO 65409.*

*Email: nathm@mst.edu

Electronic Supplementary Information (ESI) available: Raman spectra, cyclic voltammograms, LSV plots, XPS spectra and pxrd patterns after catalytic activity, and models used for DFT calculations. See DOI: 10.1039/x0xx00000x covalency in the metal-anion bonding[32], it can be expecetd that catalytic efficiency will increase in the chalcognide series. In accordance with that hypothesis, it has been observed that among the Ni-based binary chalcogenides, nickel selenides exhibit some of the best catalytic efficiency.[17,24,30-33] Since the electronegativity of Te (2.1) is lower than that of Se (2.55), the degree of covalency in nickel tellurides will be even higher than that in the selenides. In fact, qualitative band structure analysis has confirmed that tellurides indeed have better band alignment with the water oxidation levels compared to the selenides.[41,42] Hence, we propose that nickel tellurides will be even better OER electrocatalysts than the selenides. Apart from band strutcure considerations, this hypothesis is also based on the change of chemical potential of the catalytically active Ni site as a function of anion composition. In all of these Ni-based OER electrocatalysts, the catalytic Ni site is activated by a pre-oxidation step which converts Ni^{2+} to Ni^{3+}. This pre-oxidation step is influenced by the coordination environment around the Ni atom and it has been shown previously in coordination complexes that by changing the coordination from sulfide to selenide, i.e. decreasing electronegativity, the oxidation peak can be moved to more cathodic potentials.[43,44] Since the Ni oxidation plays a pivotal role in the catalytic process, it can be envisioned that lowering of the oxidation potential through increasing covalency in the coordination environment will have a positive influence in lowering the onset potential for OER thereby, increasing catalytic efficiency. In this article, we have provided the first proof of this hypothesis by investigating the OER catalytic activity of Ni_3Te_2 in alkaline electrolyte. Ni_3Te_2 was synthesized both by hydrothermal technique as well as direct electrodeposition on the electrodes. Both hydrothermally synthesized as well as electrodeposited Ni_3Te_2 showed OER catalytic activity indicating that it was indeed an intrinsic property of the material. The electrodeposited Ni_3Te_2 exhibited high catalytic efficiency requiring a very low overpotential of only 180 mV to reach 10 mA cm^{-2}, which is one of the lowest overpotentials reported till date. This overpotential is also significantly lower than that required for nanostructured Ni_3Se_2 (190 mV)[31] and Ni_3S_2 (260 mV)[29], which proves the hypothesis that increasing covalency in the chalcogenide series can indeed lead to better catalytic efficiency. Through DFT calculations we have also shown that the hydroxyl attachment to the Ni sites is energetically more favorable in Ni_3Te_2 than in NiO (NiOOH). The discovery of efficient catalytic activity in Ni-tellurides along with the trend of increasing catalytic activity in the chalcogenide series provides valuable insights that will lead us to designing highly efficient electrocatalysts by optimizing the material properties.

2. Experimental Section

2.1 Materials

All the chemicals used for the synthesis were of analytical grade and were used without further purification. All solutions were prepared using deionized water (DI : resistivity 18 MΩ cm). Nickel sulfate ($NiSO_4·6H_2O$) was purchased from Fisher Scientific, tellurium dioxide (TeO_2) and hydrazine hydrate ($N_2H_4·H_2O$, 100%) were purchased from the Acros Organics. Au coated glass slides (Au-glass, hereafter) were bought from Deposition Research Lab Incorporated (DRLI) Lebanon, Missouri.

2.2 Electrodeposition of Ni_3Te_2

Conventional three-electrode system was used for the electrodeposition of Ni_3Te_2 films on different conducting substrates (e.g. Au-glass, GC (0.196 cm^2), Ni Foam, carbon fiber paper, etc.). Ag|AgCl and Pt mesh were used as the reference and counter electrode, respectively. Substrates were cleaned by micro-90 detergent followed by sonication in mixture of isopropanol, ethanol, and deionized water. The clean and air dried Au-glass substrates were masked with a scotch tape, leaving a circular exposed geometric area of known dimensions for the electrodeposition. Electrodeposition of Ni_3Te_2 films were carried from an electrolytic bath containing 15 mM $NiSO_4·6H_2O$ and 3 mM TeO_2 maintained at 80 °C. Dilute HCl was added to adjust the pH at 2.5 . After mixing, the solution was purged for 30 minute with N_2 gas to remove all dissolved O_2 from the elcetrochemical bath. IviumStat potentiostat was used to deposit Ni_3Te_2 films at -1.05 V applied potential (*vs* Ag|AgCl). After deposition the films were thoroughly washed with DI water to remove any adsorbents from the surface of the film.

2.3 Hydrothermal synthesis of Ni_3Te_2

In a typical synthesis, $NiSO_4·6H_2O$ (9.0 mM) was dissolved in 15.0 ml of deionized water under magnetic stirring to form a homogeneous solution. After mixing the solution for 10 min, TeO_2 (6.0 mM) was added and stirred vigorously for 20 min. Finally, $N_2H_4.H_2O$ (3.0 ml) was added to the mixture and stirred continuously for another 10 min. The resulting solution was transferred to a Teflon-lined stainless-steel autoclave. The autoclave was sealed and maintained at 185 °C for 20 h, then naturally cooled to room temperature. The black product formed was centrifuged, washed several times with DI water and then with mixture of ethanol and DI water to remove impurities. The product was dried in a vacuum oven at 60°C for 24 h.

2.4 Characterization

Powder X-ray diffraction (PXRD)

The electrodeposited Ni_3Te_2 films and hydrothermally syhthesized products were characterized using powder X-ray diffraction (PXRD) using Philips X-Pert X-ray diffractometer (PANalytical, Almelo, The Netherlands) with a CuKα (1.5418 Å) radiation. For the electrodeposited film the PXRD pattern was collected from the as-synthesized Ni_3Te_2 layer on the Au–glass substrate. The deposited Ni_3Te_2 layer was very thin on the substrate, therefore, the PXRD was collected at grazing angle incidence in thin film geometry (GI mode with Göbel mirrors).

Scanning electron microscopy (SEM)

The SEM image of Ni_3Te_2 was obtained using a FEI Helios NanoLab 600 FIB/FESEM at an accelerating voltage of 10 kV and a working distance of 4.5 mm. Energy dispersive spectroscopy (EDS) along with line scan analysis was also obtained from the same SEM.

Transmission electron microscopy (TEM)

High resolution TEM images (HRTEM) and selected area electron diffraction (SAED) patterns of Ni_3Te_2 was obtained using FEI Tecnai F20. The spot size was less than 2 nm and probe current was 1.2 nA. STEM mode in the TEM was also used for imaging with camera length of 30 mm and the convergence angle of 13 mrad. Oxford ultra-thin (UTW) window EDS detector was used to detect the elements in TEM mode.

X-ray photoelectron spectroscopy (XPS)

XPS measurements of the Ni_3Te_2 were obtained through a KRATOS AXIS 165 X-ray Photoelectron Spectrometer (Kratos Analytical Limited, Manchester, United Kingdom) using the monochromatic Al X-ray source. C1s signal at 284.5 eV was used as a reference to correct all the XPS binding energies.

2.5 Electrochemical catalytic activity

The OER and HER catalytic performance were recorded by linear sweep voltammetry (LSV), cyclic voltammetry (CV) and the stability of the catalyst was obtained from chronoamperometry using conventional three electrode electrochemical cell with an IvumStat potentiostat. Ag|AgCl, Pt mesh and electrodeposited Ni_3Te_2 films on various substrates were used as reference, counter and working electrodes, respectively. All potentials acquired *vs* Ag|AgCl were converted to the reversible hydrogen electrode (RHE) by using the following equation.

$$E_{\mathrm{RHE}} = E_{\mathrm{Ag|AgCl}} + 0.059\ \mathrm{pH} + E^0_{\mathrm{Ag|AgCl}} \qquad (1)$$

Where E_{RHE} is the calculated potential *vs* RHE, $E_{\mathrm{Ag|AgCl}}$ is the experimentally measured potential *vs* Ag|AgCl reference electrode, and $E^0_{\mathrm{Ag|AgCl}}$ is the standard thermodynamic potential of Ag|AgCl at 25 °C (0.197 V), which was calibrated following standard procedures as described in supporting information. Electrochemical data were calculated using 0.08 cm^2 as the measured film deposition area, which was kept constant for all of electrodepositions.

The electrochemically active surface area of catalyst was measured by using electrochemical double layer capacitance at different scan rates (Eq. 2) and comparing the electrochemical capacitance with the specific capacitance of given catalysts (Eq. 3). Capacitive current (i_{DL}) is the product of double layer capacitance (C_{DL}) and scan rate (ν).

$$i_{\mathrm{DL}} = \mathrm{C}_{\mathrm{DL}} \times \nu \qquad (2)$$

$$\mathrm{ECSA} = \mathrm{C}_{\mathrm{DL}}/\mathrm{C}_s \qquad (3)$$

The ECSA of the catalyst was calculated using equation 3 where C_s is the specific capacitance and reported to be between 0.022 to 0.130 mF cm^{-2} in alkaline solution. In this study, we assumed the value of C_s to be 0.040 mF cm^{-2} based on previously reported Ni-based OER catalysts[6].

The Tafel slope is the important parameter to explain the electrocatalytic activity and kinetics of a given reaction and can be expressed as follows:

$$\eta = a + \frac{2.3R\mathrm{T}}{\alpha n\mathrm{F}} \log j \qquad (4)$$

where η is the overpotential, α is transfer coefficient, n is number of electron involved in the reaction, F is Faraday constant and *j* is the current density and slope is given by 2.3RT/αnF.

The turnover frequency (TOF) is another critical parameter that can be calculated to see the OER performance of a catalyst. Turnover frequency quantifies the specific activity of a catalytic centre for OER reaction under defined reaction conditions by the number of catalytic cycles occurring at the centre per unit time.

$$\mathrm{TOF} = (I)/(4 \times F \times m) \qquad (5)$$

where I is the current in Amperes, F is the Faraday constant and m is the number of moles of the active catalyst.

Faradaic efficiency of the Ni_3Te_2 catalytic film was estimated by combined ORR–OER studies obtained from bipotentiostat mode of the IviumStat using a Rotating Ring Disk Electrode (RRDE) set-up where Pt and glassy carbon (GC) were used as ring and disk electrodes, respectively. The Faradaic efficiency was calculated using equation 6.

$$\text{Faradaic efficiency} = \frac{2i_r}{i_d\mathrm{N}} \qquad (6)$$

where i_r and i_d are the measured ring and disk currents, respectively, and N is the collection efficiency of RRDE, 0.17 in this work (See supplementary information).

2.6 Electrode Preparation

To analyze the activity of hydrothermally synthesized Ni_3Te_2, a homogeneous catalyst ink was prepared by adding 7.0 mg of catalyst powder in 100.0 µL of Nafion solution (50 µl of 1 % nafion solution in 50 µl of 50% IPA in water) followed by ultrasonication for 30 min. 20 µL of the dispersion was drop casted on a confined area (0.283 cm^2) on Au-coated glass. The drop-casted film was then dried at room temperature and finally heated at 130 °C for 30 mins in an oven.

3. Results and discussion

3.1 Structural and morphological characterization

The powder x-ray diffraction (pxrd) patterns of hydrothermally synthesized as well as electrodeposited product showed the presence of Ni_3Te_2, where the diffraction peaks matched with those reported for standard Ni_3Te_2 (PDF # 04-014-3418) as shown in Fig. 1. Ni_3Te_2 crystallizes with a monoclinic crystal structure in the $P2_1/m$ space group. Both pxrd patterns showed that the product was very pure with no other noticeable impurity peaks. However, the hydrothermally synthesized product showed better crystallinity compared to the electrodeposited sample as revealed by the higher intensity of the diffraction peaks (Fig. 1a and b). Moreover, it was observed

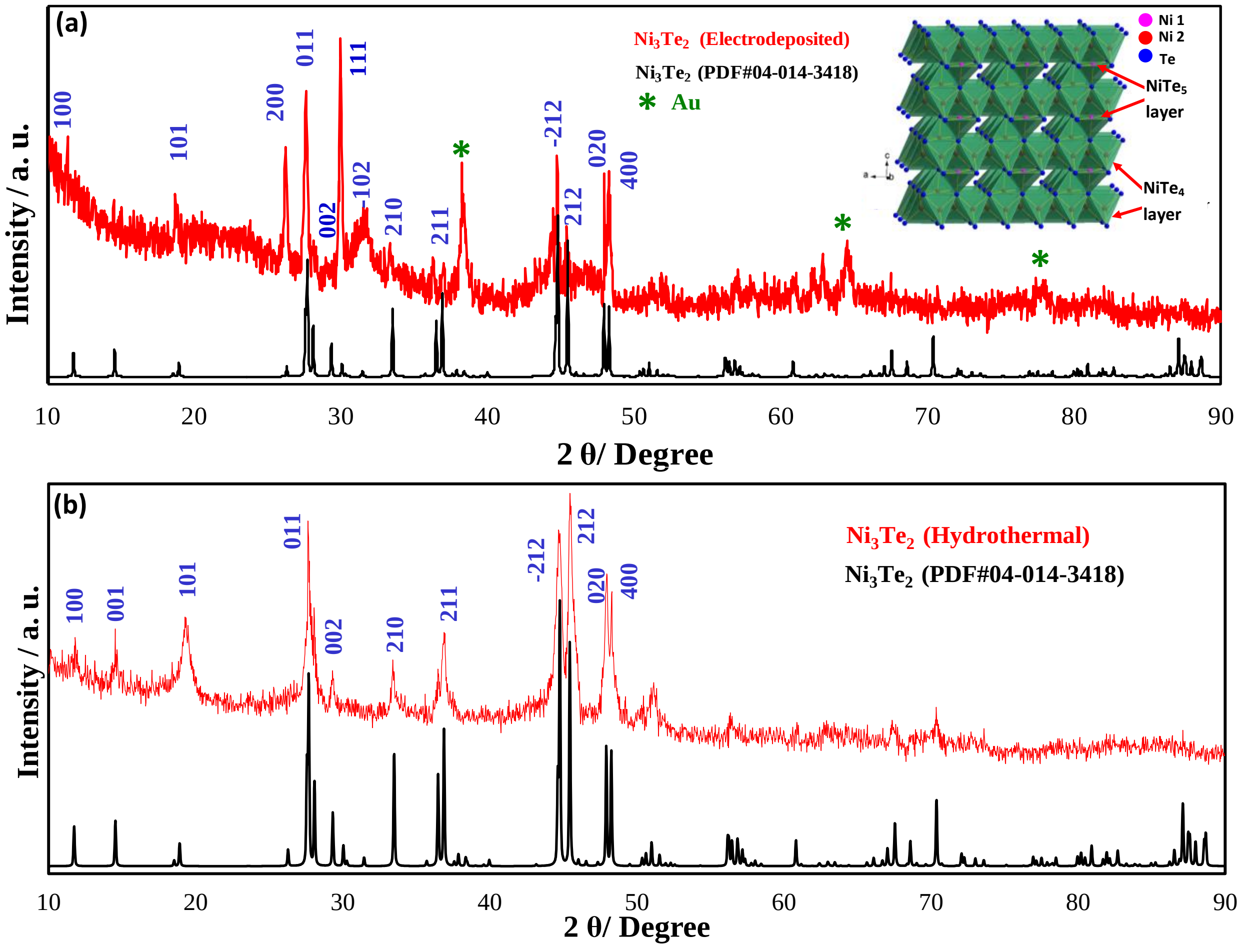

Fig. 1 PXRD patterns of (a) electrodeposited on Au and (b) hydrothermally synthesized Ni_3Te_2 catalysts along with the reference (PDF # 04-014-3418) spectrum. Inset in (a) shows the crystal structure of Ni_3Te_2 created from the corresponding cif file.

that the diffraction peaks were considerably broadened corresponding to the hydrothermally prepared Ni_3Te_2. From Scherrer equation, the average particle size was calculated to be approximately 40 nm.[45] It must be mentioned here that from pxrd studies it was apparent that there is no preferred direction of growth for either the electrodeposited or hydrothermally synthesized Ni_3Te_2. Both products contained randomly oriented nanocrystalline grains.

The crystal structure of Ni_3Te_2 is very interesting. It shows unique coordination for Ni, where two Ni atoms (Ni(2) and Ni(3)) are coordinated to 4 Te atoms in a tetrahedral geometry, while the 3rd one (Ni(1)) has a 5-coordinated square-pyramidal coordination, where Ni sites at the centre of the square planar base and the 5th Te atom occupies a vertical position atop the Ni atom with a long Ni-Te bond (inset of Fig. 1a). The $NiTe_4$ tetrahedra are connected via edge-sharing and form a continuous layer along the ab-plane. The 5-coordinated $NiTe_5$ square-pyramids are also connected through edge-sharing and the chains of such square-pyramidal $NiTe_5$ polyhedra runs along the *b*-axis, while along the *a*-axis, the $NiTe_5$ square pyramids are present as edge-shared dimeric units with each unit oriented 180° with respect to its neighbor. The periodic arrangement of the $NiTe_5$ dimeric units along the *a*-axis gives rise to a rectangular channel within the structure. The layer formed by edge-shared $NiTe_5$ polyhedra propagate along the *ab*-plane. The

$NiTe_4$ layer and the $NiTe_5$ layer are stacked alternately along the *c*-axis. The Ni(1)-Ni(2) and Ni(1)-Ni(3) distances are also quite short indicating that the structure can have several Ni-Ni metallic bonds. Interestingly due to the unique atomic arrangement and coordination geometry, at least one of the Ni atoms, Ni(1), is coordinatively under-saturated and have a vacant site available in the vertical position, which when occupied by an anion, can give rise to an octahedral geometry. The availability of such vacant site may be extremely useful for anion (e.g. OH^-) adsorption and subsequent onset of catalytic activities. The importance of NiX_4 (X = Se) polyhedra in enhancing the OER catalytic performance has also been exemplified by investigating a molecular complex containing $NiSe_4$ core,[32] The tetrahedral NiX_4 unit can possibly undergo a coordination expansion (tetrahedral to octahedral transition) initiated by hydroxyl attachment, as has been observed in coordination complexes.[46,47] It must be noted here that, although Ni_3Se_2 and Ni_3Te_2 have similar stoichiometries, their crystal structures are distinctly different indicating that their properties can also be widely varied from each other.

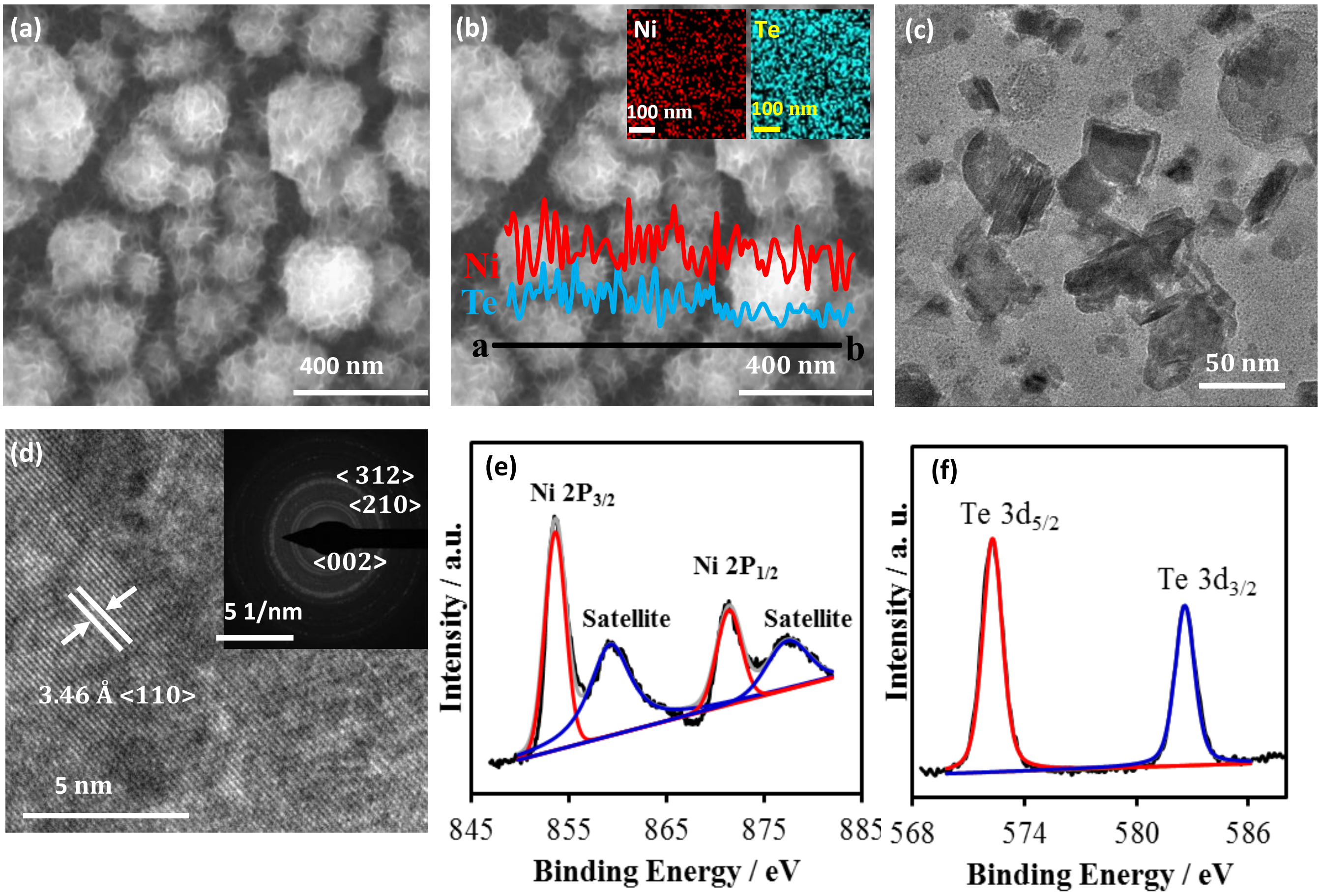

Fig. 2 Characterization of electrodeposited Ni_3Te_2 catalyst: (a) SEM image; (b) EDS mapping and line scan analysis; (c) TEM image; (d) HRTEM image. Inset of (d) shows the SAED pattern. (e) Ni 2p and (f) Te 3d XPS spectra.

The SEM image of the *as-grown* electrodeposited films showed that the surface was mainly composed of randomly oriented nanoflakes (Fig. 2a). These nanoflakes can expectedly increase the surface area of the catalytic films thereby increasing contact area between the catalyst and electrolyte. The average thickness of the flakes was estimated to be around 8 nm. TEM imaging of the electrodeposited film also showed random distribution of thin flake-like nanostructures as shown in Fig. 2c. High resolution TEM imaging revealed lattice fringes corresponding to <110> lattice planes of Ni_3Te_2 (Fig. 2d). SAED pattern collected from these nanostructures showed diffraction rings corresponding to <002>, <210>, and <312> lattice planes, which also confirmed the presence of crystalline Ni_3Te_2 in the film. SEM imaging of the hydrothermally prepared sample showed that the product was composed of nanoflakes with an average thickness of 5 nm for the nanoflakes (Fig. 3a). TEM images also confirmed the presence of thin nanoflakes in the product (Fig. 3c) while HRTEM images revealed that these nanostructures are highly crystalline with lattice fringes corresponding to <212> lattice spacing of Ni_3Te_2 (Fig. 3d). The SAED pattern showed diffraction spots corresponding to crystalline Ni_3Te_2 (inset of Fig. 3d).

The elemental composition of the electrodeposited film and hydrothermally prepared sample was further confirmed through EDS elemental mapping. While elemental mapping showed presence of Ni and Te uniformly over the sample surface (Figs. 2b and 3b), the average EDS data showed that the relative elemental composition was 62% Ni and 38% Te, revealing a relative atomic ratio of 1.5:1, confirming the formation of Ni_3Te_2. It must be noted here that there was no noticeable oxygen peak detected in the EDS spectra of either products indicating high purity of the film surface.

The surface electronic state of the Ni_3Te_2 catalyst was analyzed by X-ray photoelectron spectroscopy (XPS) and presented in Figs. 2e and 2f. The first doublet at 853.5 and 871.4 eV in Ni 2p spectra (Fig. 2e) indicated the presence of Ni^{2+} as seen in nickel telluride.[48,49] An obvious satellite peak at the higher binding energies due to the overlapping of antibonding orbital between the Ni atom and Te atom of the Ni 2p can be observed.[48] Fig. 2f shows the Te 3d spectra where the peaks at 572.3 and 582.5 eV corresponding to the $3d_{5/2}$ and $3d_{3/2}$ peaks can be assigned to Te^{2-} in nickel telluride.[48,49] It should be noted that peaks corresponding to Ni-oxides were visibly absent in the XPS spectra, indicating that the film surface was devoid of oxidic impurities. Raman spectra of as-synthesized catalyst is shown in Fig. S1 (ESI). The peaks at 108, 124 and 143 cm^{-1} can be assigned of Ni_3Te_2. There was no evidence of Ni-oxide or Te-oxide phases indicating the films were free from any oxidic impurities.

3.2 Electrochemical Characterization

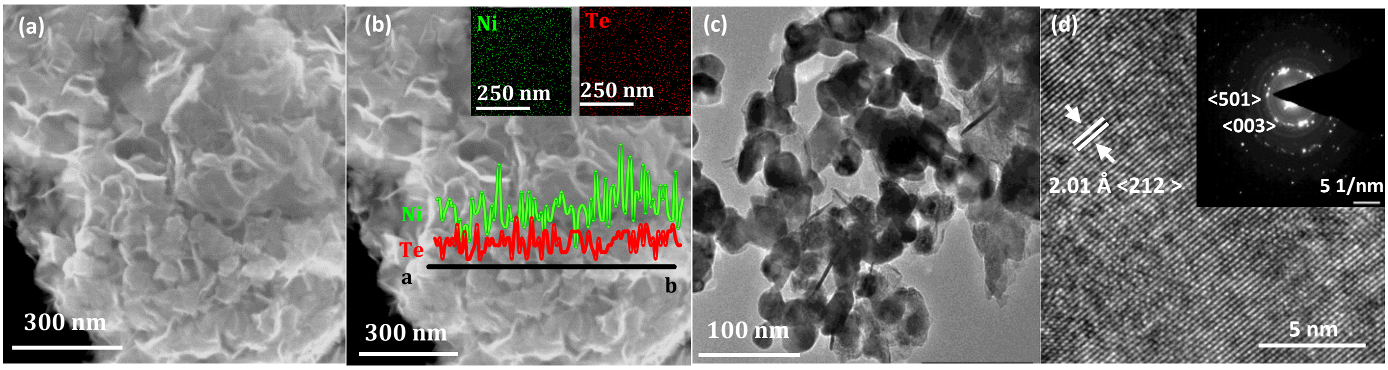

Fig. 3 Characterization of hydrothermally synthesized Ni_3Te_2 catalyst: (a) SEM image; (b) EDS mapping and line scan analysis; (c) TEM image (d) HRTEM image. Inset in (d) shows the SAED pattern from individual nanocrystallites.

The OER activity of the electrodeposited Ni_3Te_2 films were examined through electrochemical measurements in 1 M KOH. Before measuring the electrocatalytic activity, the electrochemically active surface area (ECSA) was calculated from the double layer capacitance measurement, as has been described previously.[6] Specifically, cyclic voltammograms (CVs) of the electrodeposited Ni_3Te_2 catalyst was measured from -0.35 to -0.25 V *vs.* Ag|AgCl at scan rates between 2.5 and 20 mV s^{-1} in N_2 saturated 1 M KOH as shown in Fig. 4a. The cathodic and anodic current was measured at -0.305 V *vs.* Ag|AgCl from Fig. 4a and plotted as a function of scan rates (Fig. 4b). From the average of the cathodic and anodic slopes, C_{DL} can be obtained and ECSA was calculated using Equation 3. It was observed that the electrodeposited Ni_3Te_2 films has a moderately high ECSA, 48.03 cm^2. Comparing ECSA with the geometric area gave the roughness factor. The high roughness factor of the electrodeposited film (608.0) supports the nanoflake-like geometry and might be one of the factors responsible for high catalytic activity.

3.3 OER Catalytic Activity

The electrocatalytic activity of Ni_3Te_2 was measured in N_2 saturated 1 M KOH by performing linear sweep voltammetry (LSV) as well as CVs. For fair comparison of the electrocatalytic activities, RuO_2 was electrodeposited on Au-glass using reported procedure (details have been provided in the Supplementary Information), and its OER activity was also measured. Fig. 5a shows the LSVs of electrodeposited and hydrothermally synthesized Ni_3Te_2, RuO_2 and bare Au-glass collected at a scan rate of 10 mV s^{-1}. Bare Au-coated glass did not show any OER catalytic activity as expected. However, modified Au-glass electrodes coated with electrochemically deposited and hydrothermally synthesized Ni_3Te_2 showed excellent OER catalytic activity as can be seen in Fig. 5a. The onset potential for O_2 evolution was at 1.38 V *vs* RHE for both electrodeposited and hydrothermally synthesized Ni_3Te_2. Both electrodeposited Ni_3Te_2 and hydrothermally synthesized Ni_3Te_2 showed a pre-oxidation peak before onset on catalytic activity (Fig. S2a and Fig. S3c respectively), which has been commonly observed with most Ni-based electrocatalysts containing Ni^{2+} and has been attributed to the oxidation of Ni(II) to Ni(III). Typically the OER electrocatalysts are benchmarked by comparing their overpotential, η, required to reach a current density of 10 mA cm^{-2}.[6] Since the larger oxidation peak for the electrodeposited Ni_3Te_2 masked the overpotential at 10 mA cm^{-2}, η was estimated from reverse sweep of the CV plot (Fig. S2a).

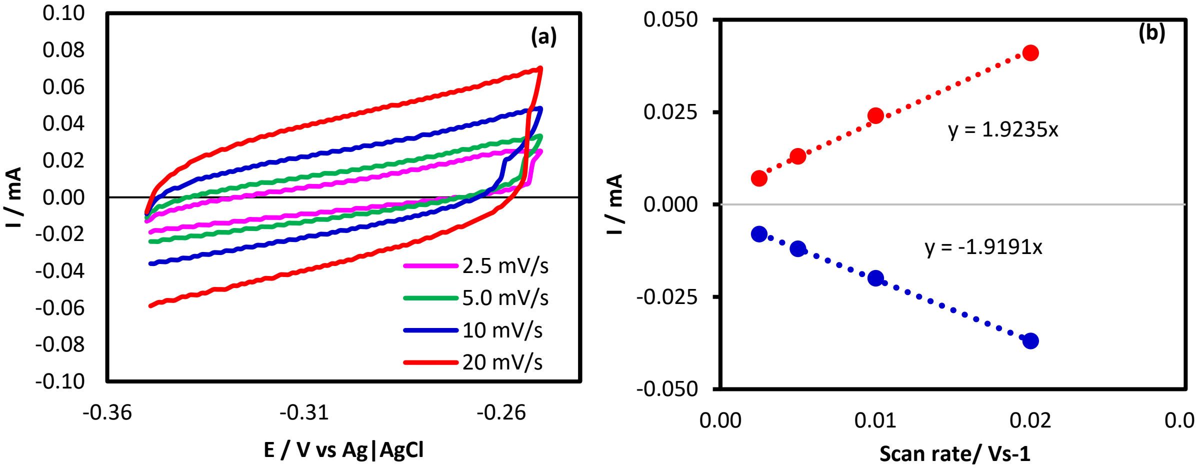

Fig.4 (a) Cyclic voltammograms measured for the electrodeposited Ni_3Te_2 catalyst on Au in N_2 saturated 1 M KOH solution at different scan rates from 2.5 to 20 mV s^{-1}. (b) Shows a plot of anodic and cathodic currents measured at - 0.305 V as a function of scan rate.

It was observed that the overpotential at 10 mA cm^{-2} was at 210 (reverse scan of CV of Fig. S2a) and 220 mV (Fig. S3c) for electrodeposited Ni_3Te_2-Au and hydrothermally synthesized Ni_3Te_2, respectively. The better OER activity for electrodeposited Ni_3Te_2 can be rationalized by considering the fact that the binder free (Nafion free) electrodeposited sample grown directly on the electrodes has better charge transport at the electrode-catalyst interface compared to the catalytic composite containing hydrothermally synthesized Ni_3Te_2 mixed with Nafion. The activity of these catalysts was compared with standard RuO_2 which shows an onset potential and η at 10 mA cm^{-2} current density at 1.51 V *vs* RHE and 370 mV, respectively, which are comparable with previous reports of RuO_2.[50] It must be noted here that this is the first example of Ni_3Te_2 showing OER catalytic activity, additionally, the onset overpotential and η are both significantly lower that other Ni-based electrocatalysts including oxides[25], sulfides[29], selenides[30] in the bulk form.

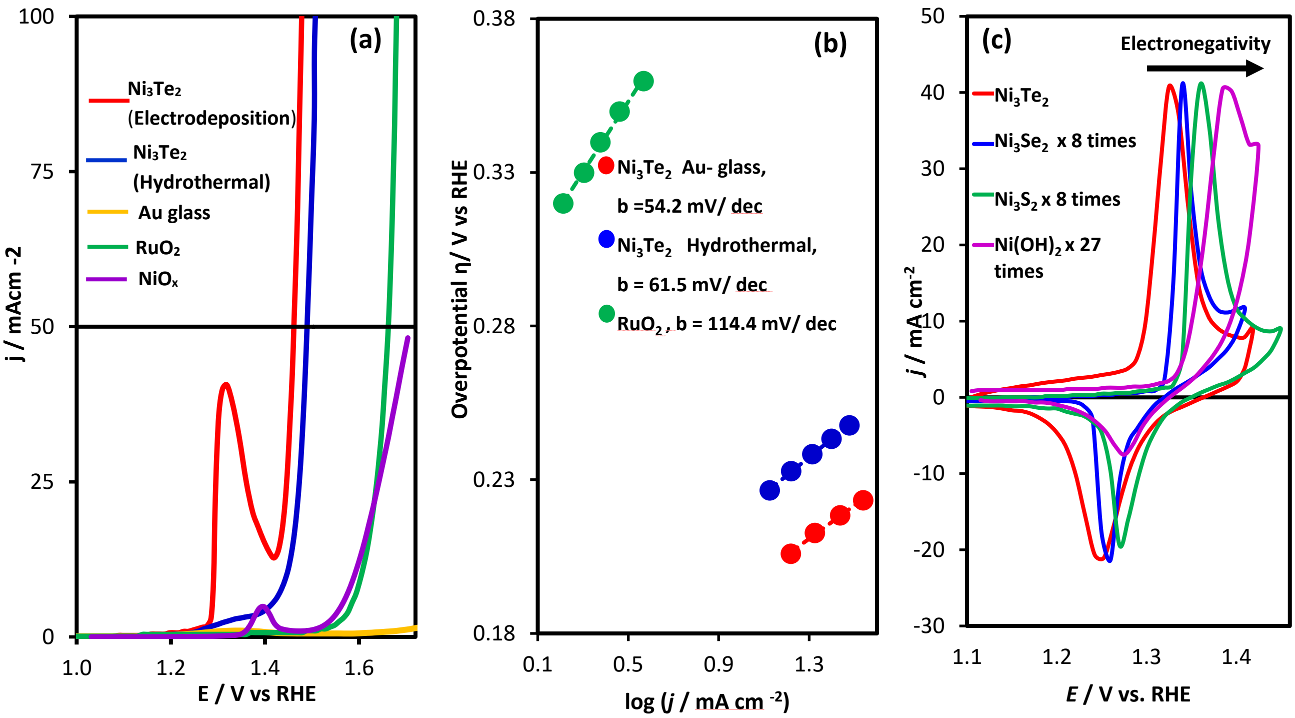

Fig.5 (a) LSVs measured for Ni_3Te_2 catalyst films in N_2 saturated 1 M KOH at a scan rate of 10 mV s^{-1}. The solid black line shows the current density at 50 mA cm^{-2}. (b) Tafel plots of both electrodeposited and hydrothermally synthesized Ni_3Te_2 compared with RuO_2. (c) Comparison of $Ni^{2+} \rightarrow Ni^{3+}$ oxidation peaks in Ni_3Te_2, Ni_3Se_2, Ni_3S_2 and $Ni(OH)_2$.

Since it has been observed in other Ni-based OER electrocatalytic system, that Fe incorporation from impure KOH can significantly boost catalytic activity, the OER activity of Ni_3Te_2 was performed in purified KOH and compared with that in impure KOH. The KOH purification was done following procedures reported previously and has been described in detail in the supporting information. However, it must be acknowledged that it is hard to remove Fe completely and presence of extremely low levels of Fe cannot be totally excluded. As shown in Fig. S3a & b, it was observed that there was no significant difference in catalytic activity between purified and impure KOH electrolyte, indicating lesser influence of Fe incorporation during OER process for Ni_3Te_2. The effect of electrodeposition time on the OER catalytic activity was probed by measuring LSV curves of Ni_3Te_2 deposited for 60s, 120s, 300s and 600s on Au/glass substrates as shown in the Fig. S4. It was observed that the OER activity gradually increased till 300 s deposition time after which the activity decreased for longer deposition times. This observation has been made earlier with electrodeposited Ni_3Se_2 electrocatalysts and can be explained from the thickness and microstructure of the film.[31] Longer deposition times typically produces thicker films which may lead to the poor electronic conductivity of semiconductor Ni_3Te_2 thus inhibiting charge transport. Lesser deposition time

Table 1: Effect of substrate on OER catalytic activity.

Substrates	Loading (mgcm^{-2})	Onset potential / V	η to 10 mA cm-2 / mV
Au glass		1.38	210
GC		1.36	180
Ni foam		1.45	230
CFP		1.41	210
C Cloth		1.42	210

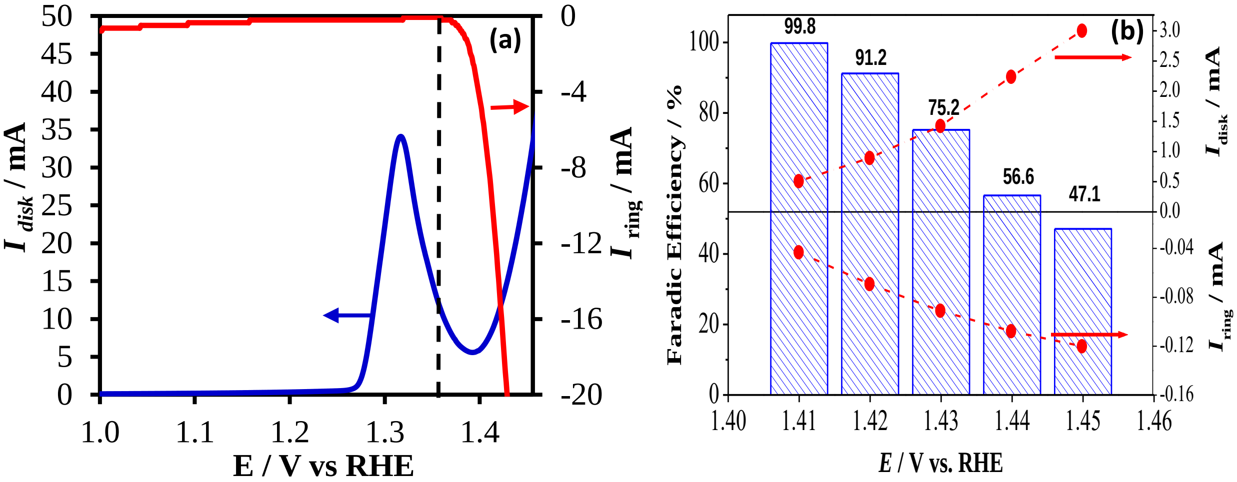

Fig.6 (a) Plots for the ORR-OER reaction showing OER current density at Ni_3Te_2 /GC disk electrode (area 0.196 cm^2) in N_2-saturated 1 M KOH and ORR current density at Pt ring electrode maintained at 0.2 V vs. RHE as a function of applied disk potential. Black line indicates the onset potential for OER at the disk electrode corresponding with the onset of ORR at the ring electrode. (b) Faradaic efficiency of catalyst measured in N_2 saturated 1 M KOH at 1600 rpm rotation speed.

on the other hand creates granular film with high roughness factor that enhances the active site exposure to the electrolytic solution thereby facilitating the catalytic process. The effect of substrate on OER catalytic activity was also investigated and the results has been summarized and presented in supplementary information (Fig.S5 and Table 1). For this study Ni_3Te_2 catalyst was deposited on glassy carbon (GC), carbon fiber paper (CFP), carbon cloth (CC), and Nickel foam (NF) for 300 s and compared with the Au-glass substrate. Among these, catalyst deposited on GC showed the lowest onset potential of 1.36 V (*vs.* RHE) and the overpotential at 10 mA cm^{-2} was only 180 mV. Surprisingly, the relatively planar substrates (GC and Au-coated glass) showed better OER activity than the porous three-dimensional substrates such as, NF, CC and CFP. This behavior can be explained by the higher loading of catalyst in three-dimensional substrate which might lead to thicker coatings with poor electronic conductivity of catalyst layer as explained earlier. Kinetics of the OER catalytic activity was investigated by analyzing the Tafel plots as shown in Fig. 5b. To obtain accurate Tafel slope values, LSVs were carried out at a slow scan speed of 2 mV s^{-1} in a non-stirred electrolyte solution. The Tafel slopes of electrodeposited and hydrothermally obtained Ni_3Te_2 were calculated as 54.2 and 61.5 mV dec^{-1}, respectively, whereas for RuO_2 it was 114.4 mV dec^{-1}. The lower Tafel slope reconfirms in the catalysts are catalytically active for OER, and using the catalyst loading as mentioned in Table 2. The TOF values were calculated to be 0.010 s^{-1} and 0.023 s^{-1} for hydrothermally synthesized and electrodeposited Ni_3Te_2 catalysts, respectively. The TOF values also indicate better OER performance for electrodeposited Ni_3Te_2.The evolved gas was analysed using RRDE experiments where Ni_3Te_2 was deposited on the disc electrode maintained as anode, while Pt ring electrode was maintained as cathode. The Pt ring was maintained at 0.2 V *vs* RHE, appropriate for O_2 reduction reaction, ORR, in alkaline condition. The idea was that if oxygen was being generated at disc electrode during anodic scan, the evolved O_2 will be promptly collected and reduced at Pt ring electrode leading to an increase in the ring current. Fig. 6 (a) shows the OER polarization curve of Ni_3Te_2 / GC disk electrode in 1 M KOH at 1600 rpm at a scan rate of 10 mV s^{-1} and ring current is presented as function of disk potential. It was observed that below the onset potential there was minimal ring current. However, as soon as disk electrode was swept past 1.36 V (onset potential), the ring current also increased indicating ORR. The ring current progressively increased as increasing disk potential. It must be mentioned here that the electrolyte solution was previously purged with N_2 and the whole experiment was performed under a blanket of N_2, thereby ensuring that there was no external source for O_2. This RRDE measurement confirmed that the evolved gas at the anode was definitely O_2.

Table 2: Comparison of electrocatalytic parameters for OER and HER

	OER						HER		
Catalysts	Total loading / mg	Loading area /mg cm^{-2}	Onset potential / V	η to 10 mA cm^{-2} / mV	TOF@ 270 mV / s^{-1}	Tafel slope / mV dec-1	Onset potential / V	η to 10 mA cm^{-2} / mV	Tafel slope / mV dec-1
Ni_3Te_2 - Au glass (ED)	0.28	4.1	1.38	210	0.023	54.2	- 0.180	237	73.1
Ni_3Te_2 - GC (ED)	0.96	4.9	1.36	180	0.010	64.3	-	-	-
Ni_3Te_2 – Hydrothermal	1.40	4.9	1.38	220	0.010	61.5	- 0.167	304	94.2
RuO_2 (ED)	-	-	1.51	370	-	114.4	-	-	-
Ni_3Te_2 – Ni foam (ED)	16.32	40.8	1.45	230	-	-	- 0.149	212	126.2
Pt	-	-	-	-	-	-	0.000	52	38.5

The Faradaic efficiency was measured from the above-mentioned RRDE experiment following procedure as detailed in supporting information. The highest efficiency was obtained to be about 99.8% which decreased with increasing disk potential (Fig. 6b). This decrease in Faradaic efficiency at relatively high disk potential is not unusual and can be attributed to poor collection at the Pt ring electrode at high potential where copious quantities of O_2 is generated. Poor collection efficiency by Pt leads to loss of undissolved O_2 resulting in lower Faradaic efficiency.[30]

At this point it is necessary to venture deeper into the cause of enhanced OER catalytic activity of Ni_3Te_2. As mentioned previously, our hypothesis was that decreasing electronegativity of the telluride anions will lead to increased covalency in the Ni-Te bonds. Such change of anion coordination is expected to alter the chemical potential around the Ni site which can be monitored by observing the redox potential of the Ni sites. In most of these Ni-based electrocatalysts catalyst activation involves Ni(II) → Ni(III) oxidation, which shows up as a pre-oxidation peak before onset of catalytic activity and it has been reported previously that Ni(III) is the actual catalytically active species. It has been observed frequently in the coordination complexes that oxidation peak potential of the central atom is lowered as electronegativity of the anions decrease down the chalcogenide series.[43, 44] We have measured the Ni (II) → Ni(III) oxidation peak in Ni_3Te_2 by collecting the CV in the range of 1.1 to 1.45 V and compared with that of Ni_3Se_2 and $Ni(OH)_2$. Indeed, it was observed that the Ni^{2+}oxidation peak showed a cathodic shift in Ni_3Te_2 indicating that the catalytically active Ni^{3+} was generated at a lower potential compared to the oxide and selenide (Fig. 5c). Availability of the catalytically active site (Ni^{3+}) at a lower potential will defnitely enhance catalytic activity by lowering the onset potential as well as overpotential for OER activity. In addition to the facile oxidation of Ni^{2+} to Ni^{3+}, the catalytic activity in Ni_3Te_2 can also be facilitated by virtue of its unique crystal structure. As explained before, Ni_3Te_2 comprises of layers containing $NiTe_4$ and $NiTe_5$ polyhedra. The $NiTe_5$ polyhedra are actually square pyramids with an open coordination site in the octahderal position, which might be viewed as functionally similar to anion vacancy. Such open coordination site might facilitate the onset of catalytic activity by readily accepting a hydroxyl ligand with minimal distortion to the existing lattice structure. Hence, enhanced availability of Ni^{3+} along with presence of accessible, coordinatively under-saturated Ni sites, collectively gives rise to unprecedented OER catalytic activity of Ni_3Te_2.

Apart from Ni^{2+} to Ni^{3+} oxidation, catalyst activation also involves attachment of hydroxyl group (OH^-) on the catalyst surface.[51] As has been reported by several groups previously, oxygen evolution reaction is initiated through the attachment of a hydroxyl (OH-) anion on the surface-active Ni site.[51] It must be mentioned here that nickel telluride surface with bound OH^- is not the same as an oxide-coated surface, but rather can be viewed as hydroxo-telluride surface akin to the oxy-hydroxide formed in the oxide surfaces. Hence, in order to study the activation of Ni_3Te_2 surface, we have estimated the simple

Table 3. A summary of adsorption energy (E_{ad}), bond distances of O-H and Ni-O (d_{O-H} and d_{Ni-O}), and angle of Ni-O-H (θ_{Ni-O-H}) for OH^- ions adsorbed on different active Ni sites in NiO and Ni_3Te_2.

Active Ni site	E_{ad} (eV)	d_{O-H} (Å)	d_{Ni-O} (Å)	θ_{Ni-O-H}
NiO_(001)_Ni	-1.608	0.964	1.808	180°
Ni_3Te_2_(001)_Ni1	-2.703	0.964	1.748	171°
Ni_3Te_2_(001)_Ni2	-2.664	0.965	1.767	172°
Ni_3Te_2_(001)_Ni3	-1.949	0.978	1.910	136°
Ni_3Te_2_(010)_Ni4	-1.820	0.979	1.825	114°
Ni_3Te_2_(010)_Ni5	-2.408	0.975	1.913	108°
Ni_3Te_2_(010)_Ni6	-2.122	0.978	1.920	115°

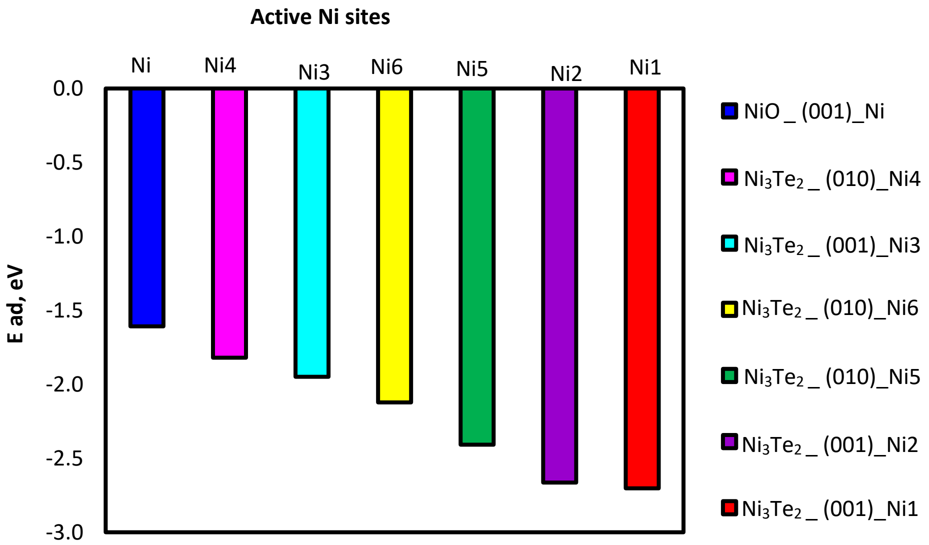

Fig.7 Adsorption energy of OH^- ions adsorbed on various active Ni sites of NiO and Ni_3Te_2. In Ni_3Te_2, Ni(1), Ni(2), Ni(4), Ni(5) correspond to tetrahedral coordination, while Ni(3), Ni(6) are square pyramidal.

hydroxyl adsorption energies (E_{ad}) through DFT by employing projected augmented wave (PAW) method, implemented in the Vienna Ab Initio Simulation Package (VASP). Details of the calculations have been provided in the supporting information. However, it must be mentioned here that OER being a multi-step process, to gain a proper understanding of the reaction kinetics on the catalyst surfaces, energetics of all the elementary steps needs to be estimated and compared. Specifically, more detailed computational-time demanding modeling study is required to determine the actual rate determining step for OER and follow the energetics to understand the catalytic efficiency as a function of composition with respect to surface energetics. We are currently expanding these DFT based calculations on a wide range of catalyst composition and trying to investigate the energetics of the different elementary steps for OER and correlate them with the catalytic efficiency in an attempt to construct the volcano-type plot. Such studies will provide a better understanding of how the OER kinetics vary on the different catalyst surfaces. These studies will be disseminated at the later time.

As has been described above, the crystal structure of Ni_3Te_2 contains three crystallographically unique Ni sites, two tetrahedral Ni sites, and one square pyramidal Ni atom. The E_{ad} value for hydroxyl attachment to each of these Ni sites has been estimated in two lattice planes, (001) and (010). The Ni sites have been designated as Ni(1)[Ni(4)], Ni(2)[Ni(5)], and Ni(3)[Ni(), for the tetrahedral and square pyramidal sites on the (001)[(010)] planes, respectively. The calculated cohesive energies of OH^- ions on (001) surface of Ni3Te2 are -2.703 eV (Ni(1)), -2.664 eV (Ni(2)), and -1.949 eV (Ni(3)), while those on (010) surface are -1.82 eV (Ni(4)), -2.408 eV (Ni(5)), and -2.122 eV (Ni(6)). The calculated data of cohesive energies, bond distances and bond angles after adsorption have been summarized in Table 3 while details of the calculation has been provided in supporting information along with illustrations depicting the crystallographic planes (Figs. S6 – S10). Interestingly, it was observed that regardless of the differences of calculated OH^- ions adsorption energies on different Ni sites in Ni_3Te_2, all of these obtained values were relatively larger than that of hydroxyl adsorption energy on a Ni-oxide surface (-1.608 eV), as can be directly observed from Fig. 7. These results suggest that surface activation of Ni site through hydroxyl attachment is more facile in Ni_3Te_2 possibly leading to more optimal coverage with OH groups at low activation potential. This factor coupled with faster generation of Ni^{3+} as shown by electrochemical data may lead to faster onset of catalytic activity at a lower applied potential. This is in very good agreement with lower onset potentials observed in the electrochemical studies, thereby providing further proof that telluride surfaces are indeed energetically more favorable for water oxidation. This study also provides information that catalytic efficiency of the Ni_3Te_2 films can be further enhanced by growing epitaxial or oriented films with preferred direction of growth, such that lattice planes with more favorable hydroxyl adsorption energy becomes the terminating plane.

3.4 Catalytic Stability

The stability of the electrocatalysts were investigated using constant oxygen evolution condition for extended period of time and cyclability of the catalyst in 1M KOH solution. Chronoamperometric studies performed for 24 h in 1 M KOH at 1.41 V applied potential is shown in Fig. 8a. It was observed that there was large amount of O_2 bubbles generated at electrode surface and hence the solution was continuously stirred at 1200 rpm to get rid of O_2 bubbles from the catalyst surface and allow progress of the reaction. As can be seen from Fig. 8a, both catalysts (electrodeposited and hydrothermally synthesized) showed exceptional stability of the OER catalytic activity for over 24h in 1 M KOH and the current density did not show any degradation. The LSV curves before and after catalytic activity were also compared to check the catalyst stability and has been shown in Fig. 8b and 8c for electrodeposited and hydrothermally synthesized catalyst, respectively. Interestingly, the LSV curves for Ni_3Te_2 after 24 h of continuous OER did not show any decrease of onset potential and overpotential compared to the as-synthesized catalysts, and the LSV curves before and after catalytic activity were perfectly superimposable.

Composition of the catalysts following catalytic activity was investigated through XPS, EDS, and pxrd analyses. XPS spectra confirmed that the elemental composition of the electrocatalyst was maintained after extended periods of catalytic activity as shown in Figs. 8e and 8f for Ni 2p and Te 3d, respectively. Noticeably the XPS peaks before and after catalytic activity did not show any shift of peak positions of Ni 2p, Te 3d (Fig. S11). As can be seen from the XPS peaks after OER activity, there was no evidence for the presence of Ni-oxidic phases, and the Te signal did not show any degradation (Figs. 6 and S11). In addition to the Ni and Te peaks, the O 1s signal was also monitored through XPS. As shown in Fig. S11, the O 1s peak showed characteristics of only surface adsorbed O_2 and traces of Te-oxides, but no Ni-oxide, which stayed the same even after prolonged period of OER. Surface morphology of the film checked through SEM imaging after activity did not reveal major changes in morphology while EDS also confirmed the presence of only Ni and Te in the film after catalytic activity, while no O was detected (Fig. S12). Fig. S13b shows the comparison of pxrd patterns for electrodeposited Ni_3Te_2 electrocatalyst before and after OER activity for 24 h. As is evident from this figure, there was no changes in peak positions after prolonged chronoamperometry in 1 M KOH, and the Ni_3Te_2 catalyst retained its bulk composition. Fig.S13a shows the Pxrd pattern of hydrothermally synthesized Ni_3Te_2 catalyst after stability and no significant difference was observed for diffraction peaks position before and after activity indicating that there was no change in the bulk composition of the catalyst.

The electrochemical stability of the catalyst surface was also probed through CV cycling in 1 M KOH. Specifically, surface oxidation has been a lingering doubt for most of these Ni-based OER electrocatalysts. If the chemical coordination around the catalytically active Ni-atoms on the surface changes drastically (such as from telluride coordination to oxide), it is expected that would lead to a change in the chemical potential and subsequently the Ni^{2+}/Ni^{3+} oxidation potential, which should be

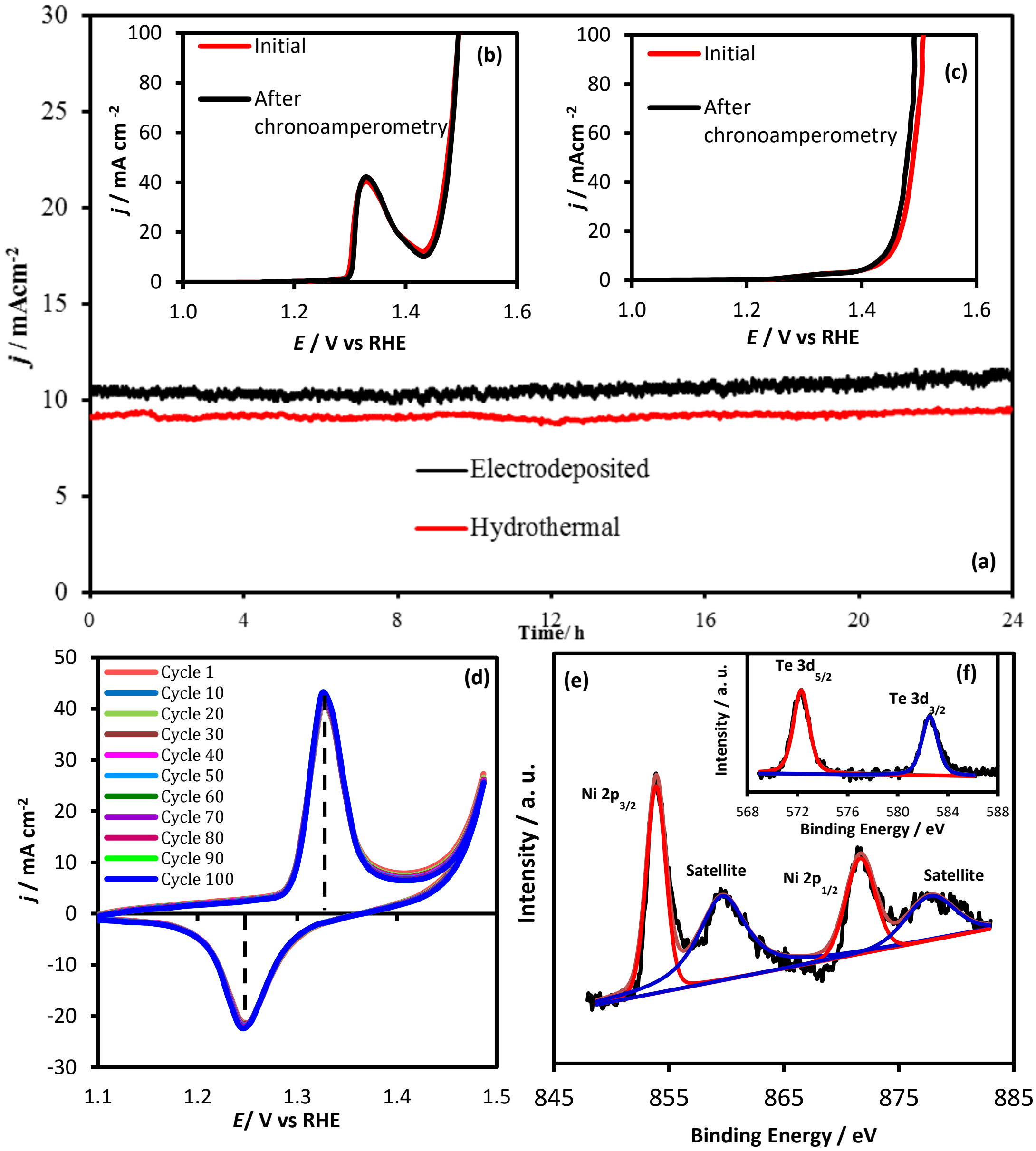

Fig.8 (a) Extended stability study of the Ni_3Te_2 catalyst under continuous O_2 evolution for 24 h studied through chronoamperometry at constant potential of 1.44 V and 1.45 V vs RHE for elecrodeposited and hydrothermal synthesis catalyst respectively. LSVs of the (b) electrodeposited, and (c) hydrothermally synthesized Ni_3Te_2 in N_2 saturated 1 M KOH before and after chronoamperometry for 24 h. (d) CVs measured for Ni_3Te_2 @ Au- glass for 100 cycles showing the $Ni^{2+} \rightarrow Ni^{3+}$ oxidation peak. (e) Ni 2p XPS spectra, and (f) Te 3d XPS spectra after chronoamperometry for 24 h.

detected through CV cycling as a shift of the oxidation peak. Interestingly, in the present case it was observed that the $Ni^{2+} \rightarrow Ni^{3+}$ oxidation peak on the Ni_3Te_2 surface does not show any shift even with 100 CV cycles and the peaks are exactly superimposable on each other as shown in Fig. 8d. If there was surface oxidation and conversion of a Ni_3Te_2 surface to Ni-oxide/oxyhydroxide surface, then the Ni^{2+}/Ni^{3+} oxidation peak would have shown a gradual shift towards more anodic potential. This conclusively proves for the first time that the telluride surface is indeed stable towards surface oxidation in alkaline medium under conditions of OER. Rather we propose that due to the structural uniqueness of Ni_3Te_2, the $Ni^{2+} \rightarrow Ni^{3+}$ oxidation is supported through partial hydroxylation leading to a (hydroxy) telluride surface where the telluride coordination remains intact, and there is coordination expansion at the Ni site.

3.5 HER Catalysis and Bifunctionality for Water Splitting

The Ni_3Te_2 has also been studied for possible HER catalytic activity in the 1 M KOH by measuring the LSV in the same three-electrode system as has been described above. Electrodeposited Ni_3Te_2 on Au-glass and Ni foam were compared with Pt for HER catalytic activity. Interestingly, both electrodeposited and hydrothermally synthesized Ni_3Te_2 showed good HER catalytic activity as shown in Fig. 9a and Fig. S16, respectively. Electrodeposited Ni_3Te_2 on Au-glass showed an onset potential for HER at 0.180 V reaching an overpotential of 237 mV at current density of 10 mA cm^{-2}. The onset potential

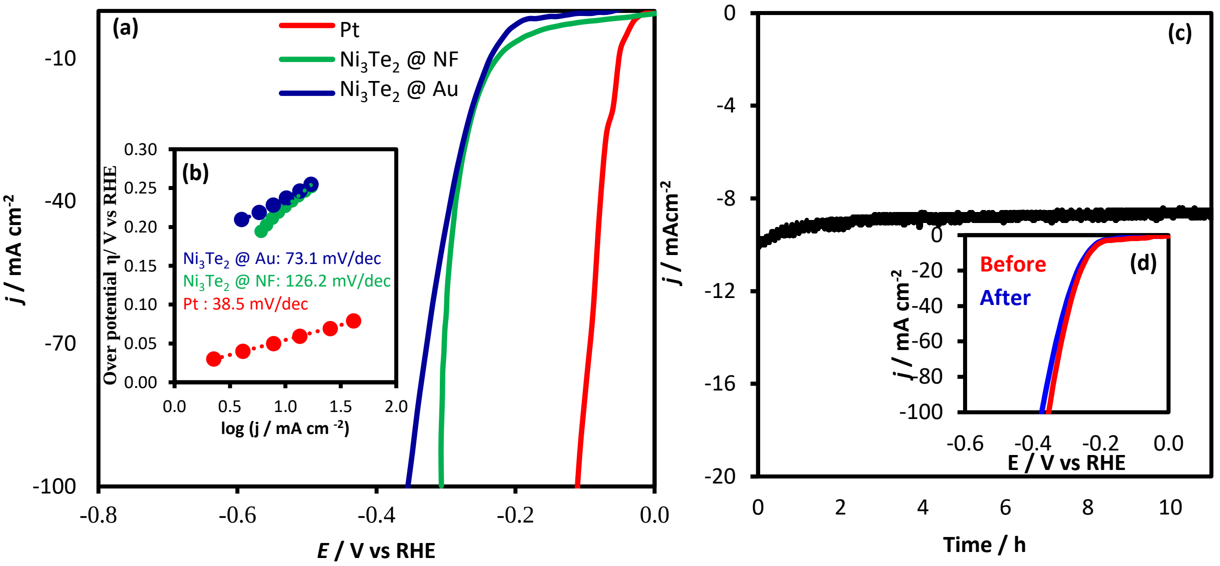

Fig.9 (a) Polarization curves for electrodeposited Ni_3Te_2 catalysts in N_2 saturated 1 M KOH solution at a scan rate of 10 mV s^{-1} under cathodic scan. (b) Tafel plots of electrodeposited Ni_3Te_2 catalysts. (c) Stability study of electrodeposited Ni_3Te_2 catalyst under continuous H_2 evolution for 11 h at constant potential of -0.237 V vs RHE. (d) LSVs of catalyst in N_2 saturated 1 M KOH for comparison of initial activity and after chronoamperometry for 11 h.

and overpotential at 10 mA cm^{-2} for the hydrothermally synthesized (Fig. S16) sample drop casted on Au-glass showed similar values (0.167V and 304 mV, respectively). The Tafel slopes were calculated from the LSV plots using equation 4 and has been plotted in Fig. 9b. The electrodeposited sample showed lower Tafel slope possibly due to more facile charge transfer on the catalyst film directly grown on the conducting electrode. The onset potential along with other parameters relevant for HER catalytic activity of Ni_3Te_2 has been listed in Table 2. The stability of the catalyst for continuous HER process in 1 M KOH was studied through chronoamperometric measurements as shown in Fig. 9c. As can be seen from the current *vs* time plot, the electrodeposited Ni_3Te_2 on Au-glass is highly stable for HER activities for extended period of time. The LSV collected after 11h of continuous HER was similar to the initial LSV plot (Fig. 9d) indicating that the catalyst did not suffer any degradation or loss of catalytic activity. The faradaic efficiency of the catalyst for the HER process was confirmed by water displacement method (details has been provided in the supplementary information). A 100% Faradaic efficiency was obtained as shown in Fig. 10. Since Ni_3Te_2 was active for both OER and HER in 1 M KOH, a full water electrolysis cell was constructed by coating Ni_3Te_2 on both cathode and anode. It was observed that Ni_3Te_2 could effectively split water producing a current density of 10 mA cm^{-2} at cell voltage of 1.62 V. The electrolysis energy efficiency was calculated to be 91.8% using standard method.[52]

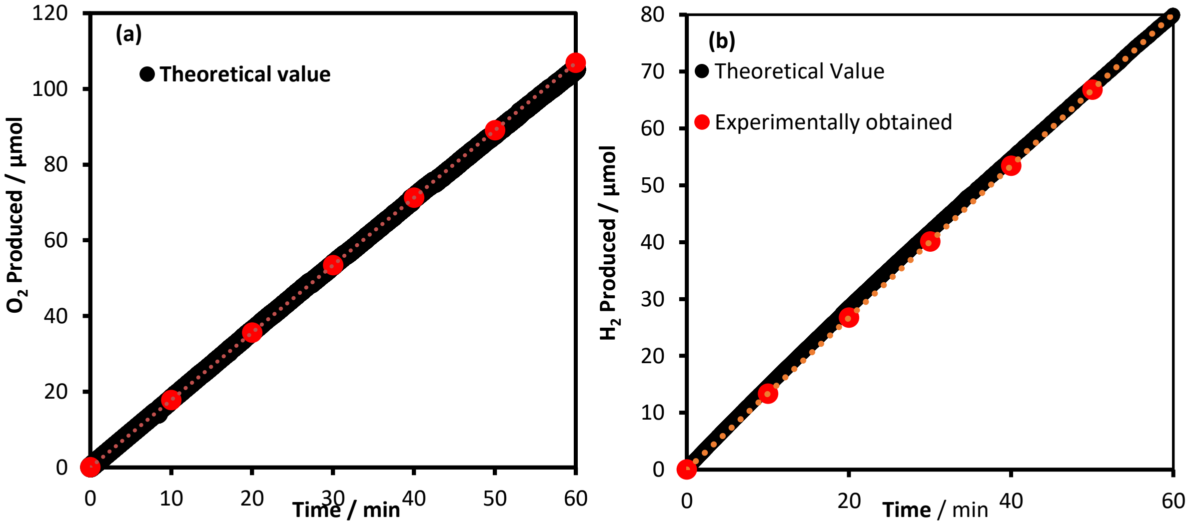

Fig.10 (a) Comparisons of experimentally obtained volumes of (a) oxygen and (b) hydrogen with the theoretically calculated amounts.

Table 4: Comparison of onset, overpotential and electronegativity values of nickel oxide and chalcogenides

	NiO_x	Ni_3S_2	Ni_3Se_2	Ni_3Te_2
η @ 10mA cm^{-2} / mV	360	330	280	180
Onset potential vs RHE / V	1.48	1.46	1.33	1.38
Electronegativity[51]	3.44	2.58	2.55	2.10

NiO , Ni_3S_2 , Ni_3Se_2 and Ni_3Te_2 catalysts were electrodeposited on Au-glass

In this report we have presented the highly efficient OER and HER electrocatalytic activity for Ni_3Te_2 in alkaline medium for the first time. The low onset potential and overpotential at 10 mA cm^{-2} for OER obtained makes this catalyst as one of the most efficient electrocatalyst for water oxidation reactions. Moreover, the activity of Ni_3Te_2 when compared to other chalcogenides in series such as Ni_3Se_2 and Ni_3S_2 shows a systematic trend of increasing activity down the chalcogenide series (Table 4, Fig. S17). This trend of increasing OER catalytic activity from oxide to telluride proves the hypothesis for the first time that increasing covalency and decreasing electronegativity of the anionic network around the transition metal center will lead to improving catalytic efficiency. Through detailed electrochemical studies we have shown that such enhancement in OER catalytic activity can be attributed to the changing redox potential of the catalytically active metal center. Hence, apart from being the first example of Ni-telluride as OER and HER electrocatalyst, this study also introduces the concept of systematically enhancing the OER catalytic activity through tuning the coordination atmosphere around the catalytically active site. Comparison with other Ni-based OER catalyst reported previously (Table 5) reveals that the Ni_3Te_2 is definitely as good as or even better than the best Ni-based OER catalyst. These findings coupled with the simple synthesis methods such as electrodeposition and hydrothermal synthesis, and possibilities to tune the catalytic efficiencies even further, makes these non-precious metal based water splitting catalysts lucrative for various energy-related practical applications.

Table 5. Comparison of the catalytic activities of Ni-based catalysts

Catalysts	Electrolytes	Loading mg cm^{-2}	Onset potential V	η @ 10 mA cm^{-2} (mV *vs* RHE)	Ref.
NiO_x nanoparticles	1M KOH	0.142	1.52*	331[b]	25
NiO_x/C	1M KOH	-	1.51*	335	20
Amorphous NiO	1 M KOH	0.1	1.54*	>470 [a]	54
α-$Ni(OH)_2$	0.1M KOH	0.2	1.54*	331	55
$Ni(OH)_2$ /NiOOH	1 M KOH	-	1.80*	525	56
$Ni(OH)_2$ nanoparticles	1M KOH	0.142	1.48*	299[b]	25
Ni_3S_2–Ni foam	0.1M KOH	37	1.387	187	27
Ni_3S_2–Ni foam	1M NaOH	1.6	1.46*	260	57
NiS/ Ni foam	1 M KOH	43	1.55	158[a]	28
NiSe–Ni foam	1M KOH	2.8	1.48*	270 [a]	33
Ni_3Se_2/Cu foam	1M KOH	3.0	1.51	343 [b]	58
$NiSe_2$ /Ti	1 M KOH	-	1.53*	320 [c]	16
$NiSe_2$	1 M KOH	1.0	1.43	250	24
$NiSe_2$-DO	1M KOH	4.1	1.46*	241	17
$NiSe_2$ /Ti	1M KOH	2.5	1.53*	295 [a]	59
Ni_3Se_2– Au Glass	0.3 M KOH	0.21	1.45	320 ±20	30
Ni_3Se_2–Ni foam		-	1.46	270 ± 20	
Ni_3Se_2 (30 s dissolution) @Au	1M NaOH	-	1.39	190	31
$Ni_{0.78}Fe_{0.22}(OH)_x$/C	0.1M KOH	0.2	1.45	290	60
$NiSe_2$ nanosheets	1MKOH	1.4	1.55	323	61
$Ni_{0.9}Fe_{0.1}O_x$	1M KOH	1.17 E-3	-	336	62
$Ni_{62}Fe_{38}O_x$ /C	0.1 M KOH	8	1.48	290	63
$Ni_{45}Fe_{55}(OOH)$	1M KOH	0.01	1.43	300	64
Ni_3Te_2– Au Glass		4.1	1.38	210 [d]	
Ni_3Te_2–Ni foam	1M KOH	40.80	1.45	230 [e]	This work
Ni_3Te_2– CFP		4.89	1.41	210	
Ni_3Te_2– C Cloth		24.81	1.42	210	
Ni_3Te_2– GC		4.9	1.36	180	
Ni_3Te_2 - Hydrothermal		4.9	1.38	220	

* Calculated from references; [a]@ 20 mA cm^{-2}; [b]@ 50 mA cm^{-2}; [c]@ 100 mA cm^{-2}, [d] supplementary figure S3a , [e] supplementary figure S3b.

Conflicts of interest

There are no conflicts to declare.

Acknowledgements

This research was supported from the National Science Foundation (DMR 1710313), the American Chemical Society Petroleum Research Fund (54793-ND10), and ERDC (Missouri S&T).

Notes and references

References

1 I. Dincer, *Renew. Sust. Energ. Rev.*, 2000, **4**, 157-175.
2 M. G. Walter, E. L. Warren, J. R. McKone, S. W. Boettcher, Q. Mi, E. A. Santori and N. S. Lewis, *Chem. Rev.,* 2010, **110**, 6446-6473.
3 L. Schlapbach and A. Züttel, *Nature,* 2001, **414**, 353-358.
4 R. Subbaraman, D. Tripkovic, K. C. Chang, D. Strmcnik, A. P. Paulikas, P. Hirunsit, M. Chan, J. Greeley, V. Stamenkovic and N. M. Markovic, *Nat. Mater.* 2012 **11**, 550-557.
5 M. T. Koper, *J. Electroanal. Chem.,* 2011, **660**, 254-260.
6 C. C. McCrory, S. Jung, J. C. Peters and T. F. Jaramillo, *J. Am. Chem. Soc.,* 2013, **135**, 16977-16987.
7 A. Marshall, B. Børresen, G. Hagen, M. Tsypkin and R. Tunold, *Energy.* 2007, **32**, 431-436.

8 P. Du and R. Eisenberg, *Energy & Environ. Sci*., 2012, **5**, 6012-6021.
9 Y. Gorlin and T. F. Jaramillo, *J. Am. Chem. Soc.,* 2010, **132**, 13612-13614.
10 M. Gong, Y. Li, H. Wang, Y. Liang, J. Z. Wu, J. Zhou, J. Wang, T. Regier, F. Wei and H. Dai, *J. Am. Chem. Soc.,* 2013, **135**, 8452-8455.
11 M. Görlin, J. Ferreira de Araújo, H. Schmies, D. Bernsmeier, S. Dresp, M. Gliech, Z. Jusys, P. Chernev, R. Kraehnert, H. Dau, and P. Strasser *J. Am. Chem. Soc.* 2017, **139**, 2070-2082.
12 M. Nath, In *Nanotechnology:* American Chemical Society, Washington DC, **2***,* 139-166, 2016.
13 J. Masud, A. T. Swesi, W. P. R. Liyanage and M. Nath, *ACS Appl. Mater. Inter.,* 2016, **8**, 17292-17302.
14 C. Xia, Q. Jiang, C. Zhao, M. N. Hedhili and H. N. Alshareef, *Adv. Mater.,* 2016, **28**, 77–85.
15 J. Luo, J. H. Im, M. Mayer, M. Schreier, M. Nazeeruddin, N. Park, S. Tilley, H. Fan and M. Gratzel, *Science,* 2014, **345,** 1593–1596.
16 T. Liu, A.M. Asiri and X. Sun, *Nanoscale,* 2016, **8**, 3911- 3915.
17 X. Xu, F. Song and X. Hu, *Nat. Commun*., 2016, **7**, 12324.
18 W. Xu, Z. Lu, X. Lei, Y. Li and X. Sun, *Phys. Chem. Chem. Phys*., 2014, **16**, 20402–20405.
19 T. Liu, Q. Liu, A. Asiri, Y. Luo, X. Sun, *Chem. Commun*., 2015, **51**, 16683-16686.
20 Y. Qiu, L. Xin and W. Li, *Langmuir.,* 2014, **30**, 7893–7901.
21 C. Tang, A.M. Asiri and X. Sun, *Chem. Commun*., 2016, **52**, 4529-4532.
22 Z. Peng, D. Jia, A. Al-Enizi, A, Elzatahry and G. Zheng, *Adv. Energy Mater*. 2015, **5**, 1402031-1402038.
23 D. Tang, J. Liu, X. Wu, R. Liu, X. Han, Y. Han, H. Huang, Y. Liu and Z. Kang, *ACS Appl. Mater. Inter.,* 2014, **6**, 7918–7925.
24 I. H. Kwak, H. S. Im, D. M. Jang, Y. W. Kim, K. Park, Y. R. Lim, E. H. Cha and J. Park, *ACS Appl. Mater. Inter.,* 2016, **8**, 5327–5334.
25 L. A. Stern and X. Hu, *Faraday Discussions* 2014, **176**, 363-379.
26 P. D. Tran, S. Y. Chiam, P.P. Boix, Y. Ren, S. S. Pramana, J. Fize, V. Artero and J. Barber, *Energy & Environ. Sci*., 2013, **6**, 2452-2459.
27 W. Zhou, X. J. Wu, X. Cao, X. Huang, C. Tan, J. Tian, H. Liu, J. Wang and H. Zhang, *Energy & Environ. Sci*., 2013, **6**, 2921-2924.
28 W. Zhu, X. Yue, W. Zhang, S. Yu, Y. Zhang, J. Wang and J. Wang, *Chem. Commun*., 2016, **52**, 1486-1489.
29 L. L. Feng, G. Yu, Y. Wu, G. D. Li, H. Li, Y. Sun, T. Asefa, W. Chen and X. Zou, *J. Am. Chem. Soc.,*2015, **137**, 14023-14026.
30 A. T. Swesi, J. Masud and M. Nath, *Energy & Environ. Sci*., 2016, **9,** 1771-1782.
31 A. T. Swesi, J. Masud and M. Nath, *J. Mater. Res.,* 2016, 1-9.
32 J. Masud, P. C. Ioannou, N. Levesanos, P. Kyritsis, and M. Nath, *Chem.Sus.Chem*.,2016, **9**, 3128-3132.
33 C. Tang, N. Cheng, Z. Pu, W. Xing and X. Sun, *Angew. Chem. Int. Edit*., 2015, **54**, 9351 –9355.
34 J. Shi, J. Hu, Y. Luo, X. Sun, and A. Asiri, *Catal. Sci. Technol*., 2015, **5**, 4954-4958.
35 C. Wang, J. Jiang, T. Ding, G. Chen, W. Xu, and Q. Yang, *Adv. Mater. Interfaces.,* 2016, **3**, 1500454.
36 K. Xu, P. Chen, X. Li, Y. Tong, H. Ding, X. Wu, W. Chu, Z. Peng, C. Wu and Y. Xie, *J. Am. Chem. Soc.,*2015, **137**, 4119-4125.
37 S.Hu, M.R. Shaner, J.A. Beardslee, M. Lichterman, B. S. Brunschwig and N. S. Lewis, *Science.* 2014, **344**, 1005-1009.
38 J. Masud, S. Umapathi, N. Ashokaan and M. Nath, *J. Mater. Chem. A.,*2016, **4**, 9750-9754.
39 M. Ledendecker, S. K. Calderon, C. Papp, H.P. Steinruck, M. Antonietti and M. Shalom, *Angew. Chem. Int. Edit*., 2015, **127**, 12538–12542.
40 Q. Liu, S. Gu and C. Li, *J. Power Sources.*, 2015, **299**, 342-346.
41 Y. Xu and M.A.A. Schoonen, *Am. Mineral*., 2000, **85**, 543-556.
42 F. A. Rasmussen and K.S. Thygesen, *J. Phys. Chem. C.,* 2015, **119**, 13169-13174.
43 C. Wombwell and E. Reisner, *Chem. Eur. J.,* 2015, **21**, 8096-8104.
44 N. Levesanos, W.P.R. Liyanage, E. Ferentinos, G. Raptopoulos, P. Paraskevopoulou, Y. Sanakis, A. Choudhury, P. Stavropoulos, M. Nath and P. Kyritsis, *Eur. J. Inor. Chem.,* 2016, **34**, 5332-5339.
45 Patterson, A.L The Scherrer formula for X-ray particle size determination. *Phys. Rev.* **56**, 978 (1939).
46 E. Ferentinos, D. Maganas, C. P. Raptopoulou, A. Terzis, V. Psycharis, N. Robertson and P. Kyritsis, *Dalton T.*, 2011, **40**, 169-180.
47 D. Maganas, J. Krzystek, E. Ferentinos, A.M. Whyte, N. Robertson, V. Psycharis, A. Terzis, F. Neese and P. Kyritsis, *Inorg. Chem.*, 2012, **51**, 7218-7231.
48 W. Bensch, W. Heid, M. Muhler, S. Jobic, R. Brec and J. Rouxel, *J. Solid. State. Chem.*, 1996, **121**, 87-94.
49 O. Rotlevi, K.D. Dobson, D. Rose and G. Hodes, *Thin Solid Films.,* 2001, **387**, 155-157.
50 M.R. Gao, X. Cao, Q. Gao, Y.F. Xu, Y.R. Zheng, J. Jiang and S.H. Yu, *ACS Nano.,* 2014, **8**, 3970-3978.
51 T. Shinagawa, A.T. Garcia-Esparza, and K.Takanabe, *Sci. Rep.UK.*, 2015, **5**, 13801.
52 A. L. Allred , *J. Inorg. Nucl. Chem.,* 1961, **17**, 215.
53 W. Kreuter and H. Hofmann, *Int. J. Hydrogen Energy,* 1998, **23**, 661-666.
54 L. Kuai, J. Geng, C. Chen, E. Kan, Y. Liu, Q. Wang and B.A. Geng, *Angew. Chem. Int. Edit*. , 2014.**53**, 7547–7551.
55 M.Gao, W. Sheng, Z. Zhuang, Q. Fang, S. Gu, J. Jiang and Y. Yan, *J. Am. Chem. Soc.*, 2014, **136**, 7077-7084.
56 S. Klaus, Y. Cai, M. Louie, L. Trotochaud and A. T. Bell, *J. Phys. Chem. C.,* 2015,**119**, 7243-7254.
57 L. L. Feng, G. Yu, Y. Wu, G. D. Li, H. Li, Y. Sun, T. Asefa, W. Chen and X. Zou, *J. Am. Chem. Soc.,*2015, **137**, 14023-14026.
58 J. Shi, J. Hu, Y. Luo, X. Sun and A. M. Asiri, *Catal. Sci. Technol.***,** 2015, **5**, 4954 - 4958.
59 Z. Pu, Y. Luo, A. M. Asiri and X. Sun, *ACS Appl. Mater. Inter.*, 2016, **8**, 4718-4723.
60 S. Dresp and P. Strasser, *ECS Transactions*, 2016, **75**,1113-1119.
61 Z. Wang, J. Li, X. Tian, X. Wang, Y. Yu, K.A. Owusu, L. He and L. Mai, *ACS Appl. Mater. Inter.*, 2016, **8**, 19386-19392.
62 L. Trotochaud, J.K. Ranney, K.N. Williams and S. W. Boettcher, *J. Am. Chem. Soc.,* 2012, **134**,17253-17261.
63 M. Görlin, M. Gliech, J.F. de Araújo, S. Dresp, A. Bergmann and P. Strasser, *Catal. Today.*, 2016, **262**, 65-73.
64 M. Görlin, J. F. de Araújo, H. Schmies, D. Bernsmeier, S. Dresp, M. Gliech, Z. Jusys, P. Chernev, R. Kraehnert, H. Dau and P. Strasser, *J. Am. Chem. Soc.,* 2017, **139**, 2070-2082.

Nickel telluride as a bifunctional electrocatalyst for efficient water splitting in alkaline medium

Mange De Silva,[a] Jahangir Masud,[a] Ning Zhang,[b] Yu Hong,[b] Wipula P. R. Liyanage,[a] Mohsen Asle Zaeem,[b] Manashi Nath[a]*

Ni_3Te_2 has been reported as a highly efficient OER electrocatalyst with an overpotential of 180 mV at 10 mA/cm^2 and also showing HER catalytic activity in alkaline medium.